Contreras, Y, Sanhueza, P, Jackson, JM, Guzman, AE, Longmore, SN, Garay, G, Zhang, Q, Nguyen-Luong, Q, Tatematsu, K, Nakamura, F, Sakai, T, Ohashi, S, Liu, T, Saito, M, Gomez, L, Rathborne, J and Whitaker, S

 Infall Signatures in a Prestellar Core embedded in the High-Mass 70 μm Dark IRDC G331.372-00.116

http://researchonline.ljmu.ac.uk/id/eprint/8639/

Article

For more information please contact researchonline@ljmu.ac.uk

INFALL SIGNATURES IN A PRESTELLAR CORE EMBEDDED IN THE HIGH-MASS 70 μM DARK IRDC G331.372-00.116

Yanett Contreras,[1] Patricio Sanhueza,[2] James M. Jackson,[3] Andrés E. Guzmán,[2, 4] Steven Longmore,[5] Guido Garay,[4] Qizhou Zhang,[6] Quang Nguyễn-Lu'o'ng,[7] Ken'ichi Tatematsu,[2] Fumitaka Nakamura,[2] Takeshi Sakai,[8] Satoshi Ohashi,[9] Tie Liu,[10, 11] Masao Saito,[2] Laura Gomez,[12] Jill Rathborne,[13] and Scott Whitaker[14]

[1] Leiden Observatory, Leiden University, PO Box 9513, NL-2300 RA Leiden, the Netherlands

[2] National Astronomical Observatory of Japan, National Institutes of Natural Sciences, 2-21-1 Osawa, Mitaka, Tokyo 181-8588, Japan

[3] School of Mathematical and Physical Sciences, University of Newcastle, University Drive, Callaghan NSW 2308, Australia

[4] Departamento de Astronomía, Universidad de Chile, Camino el Observatorio 1515, Las Condes, Santiago, Chile

[5] Astrophysics Research Institute, Liverpool John Moores University, 146 Brownlow Hill, Liverpool L3 5RF, UK

[6] Harvard-Smithsonian Center for Astrophysics, 60 Garden Street, Cambridge, MA 02138, USA

[7] The Canadian Institute for Theoretical Astrophysics (CITA), University of Toronto, 60 St. George Street, Toronto, Ontario, M5S 3H8, Canada

[8] The University of Electro-Communications, Chofu, Tokyo 182-8585, Japan

[9] RIKEN, 2-1, Hirosawa, Wako-shi, Saitama 351-0198, Japan

[10] Korea Astronomy and Space Science Institute, 776 Daedeokdaero, Yuseong-gu, Daejeon 34055, Republic of Korea

[11] East Asian Observatory, 660 N. A'ohoku Place, Hilo, HI 96720, USA

[12] Joint ALMA Observatory, Alonso de Córdova 3107, Vitacura, Santiago, Chile

[13] CSIRO Astronomy and Space Science, P.O. Box 76, Epping NSW 1710, Australia

[14] Physics Department, Boston University, Boston, MA, USA

ABSTRACT

Using Galactic Plane surveys, we have selected a massive (1200 M$_\odot$), cold (14 K) 3.6-70 μm dark IRDC G331.372-00.116. This IRDC has the potential to form high-mass stars and, given the absence of current star formation signatures, it seems to represent the earliest stages of high-mass star formation. We have mapped the whole IRDC with the Atacama Large Millimeter/submillimeter Array (ALMA) at 1.1 and 1.3 mm in dust continuum and line emission. The dust continuum reveals 22 cores distributed across the IRDC. In this work, we analyze the physical properties of the most massive core, ALMA1, which has no molecular outflows detected in the CO (2-1), SiO (5-4), and H$_2$CO (3-2) lines. This core is relatively massive ($M = 17.6$ M$_\odot$), subvirialized (virial parameter $\alpha_{vir} = M_{vir}/M = 0.14$), and is barely affected by turbulence (transonic Mach number of 1.2). Using the HCO$^+$ (3-2) line, we find the first detection of infall signatures in a relatively massive, prestellar core (ALMA1) with the potential to form a high-mass star. We estimate an infall speed of 1.54 km s^{-1} and a high accretion rate of 1.96×10^{-3} M$_\odot$ yr^{-1}. ALMA1 is rapidly collapsing, out of virial equilibrium, more consistent with competitive accretion scenarios rather than the turbulent core accretion model. On the other hand, ALMA1 has a mass $\sim$6 times larger than the clumps Jeans mass, being in an intermediate mass regime ($M_J = 2.7 < M \lesssim 30$ M$_\odot$), contrary to what both the competitive accretion and turbulent core accretion theories predict.

Keywords: ISM: clouds — ISM: individual objects (IRDC G331.372-00.116) — ISM: molecules — ISM: kinematics and dynamics — stars: formation

Corresponding author: Yanett Contreras
ycontreras@strw.leidenuniv.nl

arXiv:1805.01802v1 [astro-ph.GA] 4 May 2018

1. INTRODUCTION

Stars form from dense ($\sim10^6$ cm^{-3}), compact ($\sim0.05-0.1$ pc) self-gravitating regions, or 'cores', that are embedded in extended, usually filamentary, clumps of molecular gas (~1 pc). While the formation of low-mass stars is relatively well understood, the formation of high-mass stars (>8 M$_\odot$) remains shrouded in uncertainties. One of the main questions about the formation of high-mass stars is how they gather their initial mass. To answer this, one requires to measure the initial condition of the gas within cores that have not yet formed high-mass stars. At later evolutionary stages, the outflows, stellar heating, and ionization from the newly formed stars will affect its environment making it more difficult to study their mass accretion mechanisms.

Currently, two main scenarios aim to explain how high-mass stars acquire their mass (see review by Tan et al. (2014)). In the 'competitive accretion' theory (Bonnell et al. 2001), at early times a molecular cloud fragments into a swarm of small cores, each with a mass roughly equal to the thermal Jeans mass (~2 M$_\odot$ at a volume density of 5×10^4 cm^{-3} and a temperature of 12 K). As gas funnels down the gravitational potential well of the much larger molecular clump, those cores near the center of the potential receive a fresh supply of gas from afar and grow via Bondi-Hoyle accretion. In this scenario it is expected to see signatures of global collapse in the ambient gas, which would suggest that material is being funneling into the cores (e.g. Peretto et al. 2013; Liu et al. 2013, 2016).

On the other hand, in the 'turbulent core accretion' scenario (McKee & Tan 2003), cores are fed only locally. In this theory, all of the mass accreted onto the final high-mass star originates locally, at birth, within the core (Tan et al. 2014). One of the main observational predictions of 'turbulent core accretion' is the presence of high-mass prestellar cores (>30 M$_\odot$, necessary to form a 8 M$_\odot$ star assuming a star formation efficiency of 30%). However, there is a of lack of evidence regarding the existence of these prestellar cores. The best candidates found so far correspond to G11.920.61-MM2 (Cyganowski et al. 2014), G11P6-SMA1 (Wang et al. 2014), and C1-S (Kong et al. 2017). G11.920.61-MM2 has a mass of ~30 M$_\odot$ but lack emission from molecular lines, making it very peculiar. G11P6-SMA1 has a mass of 27.9 M$_\odot$ and shows no outflow emission making it a good pre-stellar core candidate. C1-S has a mass ranging between 11 and 53 M$_\odot$, due to the uncertainty in their temperature values, which range between 7 and 13 K.

In this paper, we present observations of the massive, 70 μm dark IRDC G331.372-00.116 obtained with the Atacama Large Millimeter/submillimeter Array (ALMA). This IRDC has all the characteristics of a high-mass stellar cluster candidate in the prestellar phase. We present the ALMA 1.1 mm dust continuum emission for the whole cloud, but focus on the remarkable physical properties of the brightest core. Given the unprecedented angular resolution and sensitivity provided by ALMA at relatively high excitation transitions, we have detected infall signatures traced by HCO$^+$ (3-2) in a subvirialized prestellar, relatively massive core.

2. IRDC G331.372-00.116

G331.372-00.116 is located in the Galactic plane, in the RCW 106 complex (Nguyễn et al. 2015), at a distance of 5.4 kpc (Whitaker et al. 2017). It was detected via its bright continuum emission at 870 μm in the AT-LASGAL survey (AGAL331.372-00.116, Contreras et al. 2013). It appears as a dark silhouette against the bright diffuse IR background in the *Spitzer* 3.6 μm, 4.5 μm, 8 μm GLIMPSE (Churchwell et al. 2009), and 24 μm MIPSGAL (Carey et al. 2005) images (see Figure 1). It also appears as dark in the 70 μm PACS Herschel image, suggesting that the temperature of this clump is low. Indeed, using dust continuum emission from Herschel PACS and SPIRE images, and ATLASGAL at 870 μm, Guzmán et al. (2015) derive a dust temperature for G331.372-00.116 of 14$\pm$4 K.

G331.372-00.116 consists of a single clump with a mass (M) of 1200 M$_\odot$[1] and an effective radius of 0.56 pc, resulting in an average volume density of 2.4×10^4 cm^{-3} and a surface density of 0.26 gr cm^{-2} (Contreras et al. 2017). Assuming a 30% star formation efficiency, this clump should form a stellar cluster of 360 M$_\odot$. Making two different estimations following the empirical relation from Larson (2003) and the IMF from Kroupa (2001), a stellar cluster of 360 M$_\odot$ should host a high-mass star of 17 and 24 M$_\odot$, respectively (Equations 1 and 2 in Sanhueza et al. 2017). The virial mass (M_{vir}) of this clump is 760 M$_\odot$, based on the single-dish Mopra observations of the N$_2$H$^+$(1-0) transition with a line width of 3.0$\pm$0.2 km s^{-1} (value typically measured in IRDCs; Sanhueza et al. 2012) obtained from the Millimetre Astronomy Legacy Team 90 GHz (MALT90) Survey (Rathborne et al. 2016; Jackson et al. 2013; Foster et al. 2013, 2011). The virial parameter is $\alpha_{vir} = M_{vir}/M = 0.6$, suggest-

---

[1] This value differs from the 1640 M$_\odot$ derived in Contreras et al. (2017) due to contamination in the dust emission from a second velocity component, undetected in the MALT90 data, located in the clump's upper region. Based on the C^{18}O emission, we estimate that the clump has a mass corresponding to the 75% of the 1640 M$_\odot$ previously estimated.

ing that the clump embedded in this IRDC is gravitationally bound.

Overall, the massive IRDC G331.372-00.116 has all physical properties needed to form a stellar cluster containing at least one high-mass star.

3. OBSERVATIONS

The observations were made with ALMA, located in the Llano de Chajnantor, Chile. We used two ALMA datasets obtained during ALMA Cycle 2 (Project ID: 2013.1.00234.S; PI: Gomez) and Cycle 3 (Project ID: 2015.1.01539.S; PI: Sanhueza) that covered the continuum and molecular line emission.

The first dataset was obtained during June 2014 and May 2015. The 12 m array consisted of 34 antennas, with baselines ranging from 15 to 348 m. Large-scale continuum and line emission was recovered by including the Atacama Compact Array (ACA) using the 7 m and Total Power (TP) arrays. The 7 m array observations consisted of 9 antennas, with baselines ranging from 8 to 48 m. For both 12 and 7 m arrays, the flux calibration and phase referencing were carried out using J1427-421 and J1617-5848, respectively. For the TP observations flux calibration was done using Uranus.

The whole IRDC was covered by a 12-pointing mosaic using each array (12 and 7 m). The angular resolution of the combined images is $1\rlap.{''}2$ (0.03 pc at 5.4 kpc) and the largest angular scale recovered for the continuum emission corresponds to 39" (1 pc at 5.4 kpc). For the line emission, interferometric and single-dish (TP) data were combined.

The receiver setup corresponds to the Band 6 of ALMA centered at $\sim$267 GHz. We observed 16 spectral windows in dual polarization mode, with a bandwidth of 234 MHz. The velocity resolution of the spectral windows range between 0.5 and 1.2 km s^{-1}. Our setup targeted the optically thick transitions HCO$^+$ (3-2) and HNC (3-2) and covered the following molecular lines that were not detected: HC^{18}O$^+$ (3-2), the deuterated molecule NHD$_2$ 4(2,2)-4(1,3), and the high-excitation energy or shock-tracing lines H$_2$CS 8(1, 8)-7(1, 7), SO$_2$ 4(3-1)-4(2-2) and SO$_2$ 5(3,3)-5(2-4).

All data reduction was performed using the CASA software package (McMullin et al. 2007). Each individual dataset was independently calibrated before being merged. The 12 and 7 m array datasets were concatenated and cleaned together using the CASA `tclean` algorithm with a Briggs weighting of 0.5. To avoid artifacts due to the complex structure seen in the continuum, we used a multi-scale clean, with scale values of 0, 3, 10 and 30 times the image pixel size (0.16"). To create the continuum image, all the line free channels were

used. The 12 and 7 m array line emission was combined with the TP observations through the feathering technique. The achieved rms of the continuum is 0.06 mJy. For the lines we used the `yclean` script that automatically cleaned each map channel with custom made masks (see Appendix A). The achieved rms for the lines is 0.06 K at a velocity resolution of 0.5 km s^{-1}.

The second dataset was obtained during January 2016 and June 2016. The 12 m array consisted of 48 antennas, with baselines ranging from 15 to 331 m. Large-scale continuum and line emission was also recovered thanks to the inclusion of the ACA and TP arrays. The 7 m array observations consisted of 8 antennas, with baselines ranging from 8 to 44 m. Flux calibration was done using Ganymede for the 12 m array observations, and Ganymede, J1256-0547 and J1924-2914 for the 7 m array observations. Phase referencing was done using J1603-4904 for the 12 and 7 m arrays. For the TP observations, flux calibration was done using Uranus.

The IRDC was covered by a 10-point mosaic using the 12 m array and a 3-pointing mosaic using the ACA. The angular resolution of the images is $1\rlap.{''}2$ and the largest angular scale recovered corresponds to 43" (1.1 pc at 5.4 kpc, for the continuum emission).

The receiver setup corresponded to the Band 6 of ALMA centered at $\sim$224 GHz in dual polarization mode. The velocity resolution of the spectral windows ranged between 0.17 km s^{-1} and 1.3 km s^{-1}.This setup covered the H$_2$CO (3-2), SiO (5-4), CO (2-1), N$_2$D$^+$ (3-2), DCO$^+$ (3-2), and C^{18}O (2-1) molecular lines. In this paper we focus in the N$_2$D$^+$ (3-2), DCO$^+$ (3-2), and C^{18}O (2-1) transitions.

All data reduction was performed following the same procedure as for the previous dataset. The achieved rms of the continuum is 0.1 mJy. For the lines the achieved rms is 0.14 K at a velocity resolution of 0.08 km s^{-1}.

In what follows, all sensitivities given for both ALMA data sets and the analysis correspond to the combined array data sets (without the TP for the continuum emission). For the dust analysis we used only the Cycle 2 data at 267 GHz as it has better sensitivity.

4. RESULTS

4.1. *Dust Structure and Core Detection using Continuum Emission*

Figure 2 shows the distribution of the 1.1 mm (267 GHz) dust continuum emission obtained with ALMA. A total of 22 cores are detected above the 5σ level embedded in the $\sim$1.6 pc long filament. Cores are defined and their fluxes extracted by using the dendrogram tech-
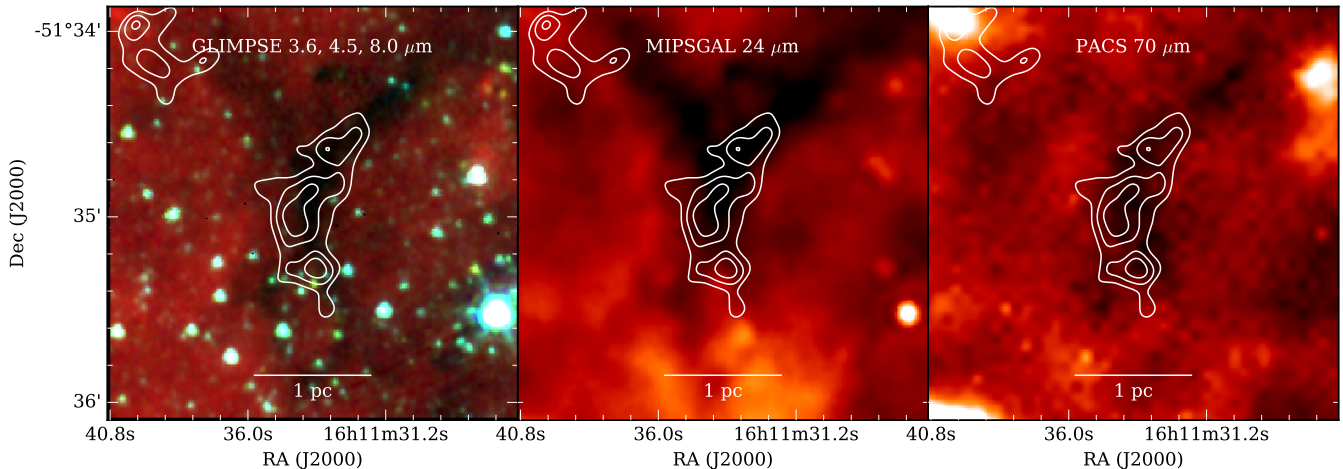
Figure 1. Infrared emission toward G331.372-00.116. G331.372-00.116 appears as a dark feature even up to 70 μm, confirming the early stage of evolution of this clump. *Left panel*: Three color image of the *Spitzer* GLIMPSE bands (Blue: 3.6 μm, green: 4.5 μm, and red: 8 μm). *Middle panel*: *Spitzer* MIPSGAL 24 μm infrared emission. *Right panel*: *Herschel* PACS 70 μm emission. In all the panels the 70% to 90% of the peak dust continuum emission from ATLASGAL is overlaid in white contours.

nique (Rosolowsky et al. 2008)[2]. Most of the cores are not isolated. They rather appear connected by more diffuse material that is recovered by the ACA array. The continuum emission revealed by ALMA generally follows the structure of the single-dish observations (elongation and curvature). The central region of the IRDC fragments in several cores, but remarkably the brightest core in the whole IRDC is located in the southern region. The discrepancy seen between the single dish and ALMA observations is seen in both epochs of ALMA observations. It can be explained by the great amount of extended diffuse emission in this IRDC that was not recovered by ALMA. Indeed only 10% of the flux observed by the single dish was detected by the 12 and 7 m ALMA arrays combined.

The mass of the cores is calculated by using the following expression:

$$M = \mathbb{R} \, \frac{F_\nu D^2}{\kappa_\nu B_\nu(T)} \, , \qquad (1)$$

where F_ν is the measured integrated source flux, $\mathbb{R}$ is the gas-to-dust mass ratio, D is the distance to the source, κ_ν is the dust opacity per gram of dust, and B_ν is the Planck function at the dust temperature T. Assuming a dust emissivity index (β) of 1.7 and scaling the value of 0.9 cm^2 g^{-1} for $\kappa_{1.3mm}$, which corresponds to the opacity of dust grains with thin ice mantles at gas densities of 10^6 cm^{-3} (Ossenkopf & Henning 1994), we obtain

$\kappa_{1.1mm} = 1.13$. A gas-to-dust mass ratio of 100 is assumed in this work. For the cores, we have adopted the *Herschel* dust temperature ($T = 14$ K) determined at the clump scale by Guzmán et al. (2015). Given that the temperature has been determined on scales much larger than the cores, this temperature represents a lower limit if deeply embedded star formation activity exists in the cores. If the cores are genuinely prestellar then the core temperature might be lower than this, and therefore the *Herschel* value would represent an upper limit. Using this dust temperature, we derive core masses ranging from 0.8 to 17.6 M$_\odot$. Based on the uncertainty analysis of Sanhueza et al. (2017), we estimate that core masses, densities, and surface densities have $\sim$50% uncertainty.

The number density is calculated by assuming a spherical core and using the molecular mass per hydrogen molecule (μ_{H_2}) of 2.8 (Kauffmann et al. 2008). Table 1 summarizes the physical properties derived for all the cores identified in G331.372-00.116.

In this work, we focus on the physical properties of the most massive core, ALMA1, and defer the analysis of the whole IRDC to a future paper.

Figure 3 shows the region surrounding ALMA1. The core is resolved at 1$''$2 resolution. Using the dendrogram technique, we derive a flux and deconvolved FWHM size of 26.0 mJy and 3$''$77$\times$2$''$64, respectively. The geometric mean of the major and minor axis is 3$''$15. The effective radius ($r_{eff} = \sqrt{A/\pi}$) is 1$''$57, i.e., 0.041 pc ($\sim$8500 AU) at the distance of 5.4 kpc, where A is the area of the ellipse determined via the dendrogram. The mass (M), number density (n(H_2)), and surface density ($\Sigma = M/(\pi r^2)$) of ALMA1 are 17.6 M$_\odot$, 0.85$\times 10^6$ cm^{-3}, and

---

[2] To compute the dendrogram we used a threshold of 10 $\times$ rms, a step of 1 $\times$ rms, and a minimum number of pixels equals to the beam's area divided by the pixel size.
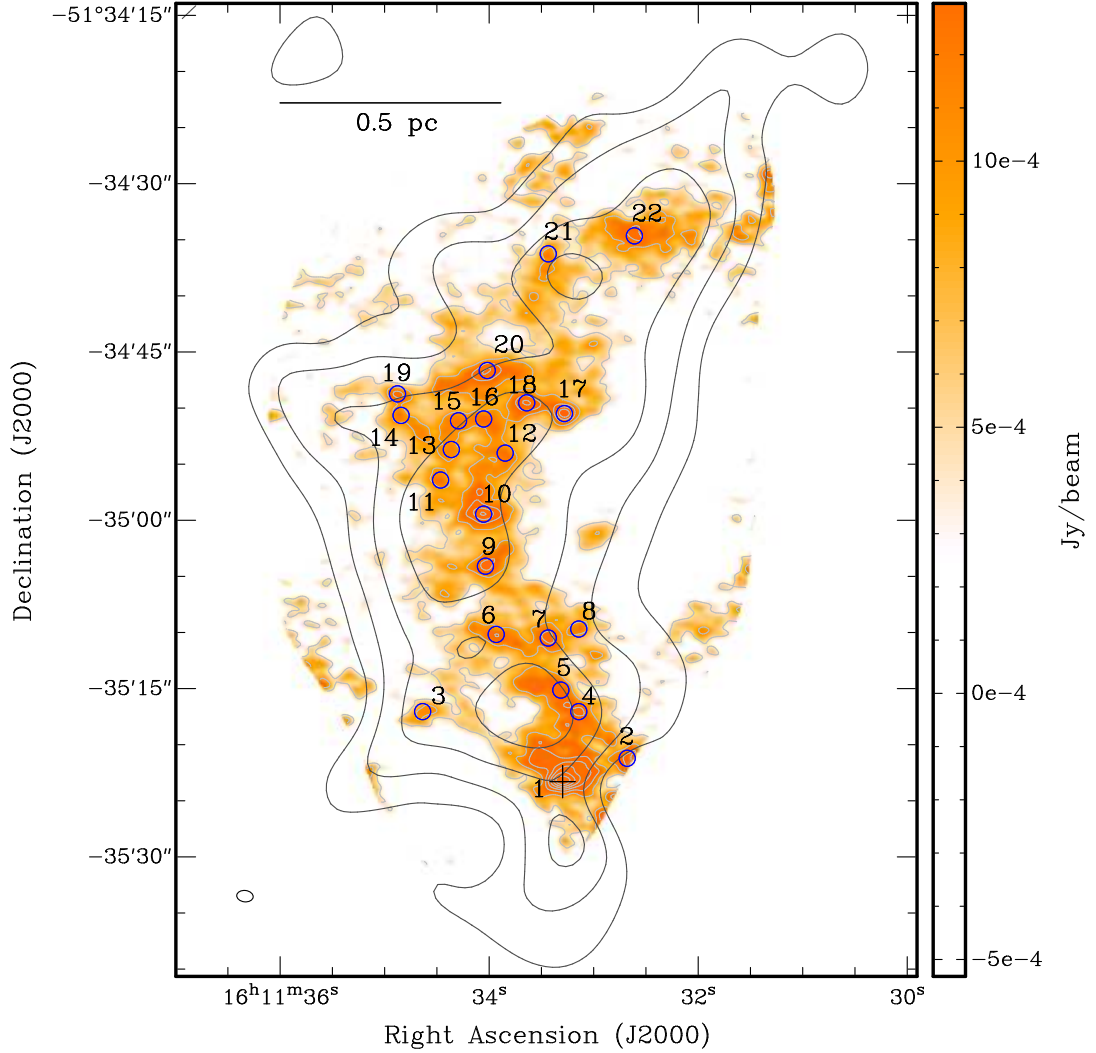
Figure 2. Dust continuum emission at 1.1 mm (267 GHz) toward G331.372-00.116. Overlaid in contours is the ATLASGAL dust continuum emission (60% to 90% of the peak emission). The ALMA beam is shown in the lower left corner of the images. The cross shows the position of ALMA1 and the rest of the cores identified are marked by blue circles with their respective number. This images shows that the overall emission recovered by ALMA follows well the shape and elongation of the ATLASGAL emission. However, although there are several cores at the center of the map, the most massive core is located in the lower part of the IRDC, not being coincident with the peaks observed in the ATLASGAL images. We recovered the same core distribution on our ALMA observations carried out during 2013 and 2015. These observations were conducted independently, confirming that there is no error on the coordinates of the ALMA images.

0.65 gr cm^{-2}, respectively. At these scales, we would expect from ALMA1 to form a single or a few stars at most, as suggested from the fragmentation scales of $\sim$ 2000 AU seeing in numerical simulations (e.g., Krumholz 2012).

We compare the core properties derived by using dendrograms with the properties obtained by fitting a 2-D Gaussian with the CASA software package. We obtain a flux of 21.9±1.6 mJy and a deconvolved FWHM size of $(3''.5\pm0''.3)\times(2''.1\pm0''.2)$, both comparable to the values

obtained with dendrograms ($\sim$15% different). Using the 2-D Gaussian values, we obtain a mass of 14.9 M$_\odot$, density of 1.2 $\times10^6$ cm^{-3}, and surface density of 0.75 gr cm^{-2}. For this work, we have adopted the values obtained via the dendrogram technique.

4.2. *Line Emission: Infall Signatures*

Figure 4 displays the observed HCO$^+$ (3-2) and C^{18}O (2-1) spectra across ALMA1, and the mean and peak HCO$^+$ (3-2), DCO$^+$ (3-2), HNC (3-2), N$_2$D$^+$ (3-2) spectra toward ALMA1. The HCO$^+$ and HNC profiles show
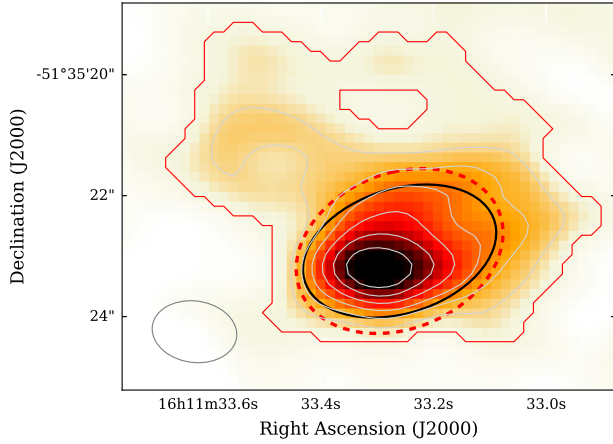
Figure 3. Dust continuum emission at 1.1 mm toward ALMA1. Overlaid in contours is shown the 40% to 90% of the dust continuum emission. The red contour shows the area of the leaf defined by the dendrogram. The dashed red ellipse shows the area representing the first and second moments of the structure determined by the dendrogram. The black ellipse shows the 2-D Gaussian fit obtained with CASA. The beam is shown in the lower left corner of the image.

a self-absorbed profile at the systemic v_{lsr} (-87.7 km s^{-1}) of the core, which is determined by the central velocity of the deuterated molecules (N_2D^+ and DCO^+). The HCO^+ spectra show a blue-red asymmetry with the blue-shifted peak brighter than the red-shifted peak. This profile is typically explained as a sign of infall, assuming the inner gas in the core has a warmer excitation temperature than the envelope. The profile of the optically thin tracers (N_2D^+, DCO^+) peak at the velocity of the self-absorption, confirming that the double-peaked profile is not due to two velocity components along the line of sight. A warmer excitation temperature in the inner region of the prestellar core can be explained by the high critical densities of the HCO^+ and HNC (3-2) transitions, 1.1×10^6 and 2×10^6 cm^{-3}, respectively. The core (average) density is 0.85×10^6 cm^{-3}, similar to the critical density of the infall tracers. At the center of the core, the density can be higher and the HCO^+ and HNC emission can be thermalised; on the other hand, in the envelope the gas density can be lower than 10^6 cm^{-3}, making the emission from the J=3-2 transitions sub-thermal with lower excitation temperatures than at the center. Although the HNC line displays a self-absorbed profile similar to the HCO^+ line, the blue- and red-shifted peaks have similar intensity and sometimes the blue-red asymmetry is reversed with the red peak slightly brighter than the blue peak. Some works (e.g., Redman et al. 2004) suggest that core rotation

and outflow activity can produce both kinds of asymmetries. We rule out the presence of molecular outflows by inspecting the CO (2-1), SiO (5-4), and H_2CO (3-2) lines, as well as the HCO^+ and HNC (3-2) lines. We detect no high-velocity gas that would indicate molecular outflows originated from ALMA1, and thus confirm its prestellar nature.

As seen in Redman et al. (2004), rotation would produce blue-red asymmetries with brighter blue peaks on one side of the core's axis of rotation and brighter red peaks on the other side. This asymmetry pattern is not observed in ALMA1. Furthermore, no velocity gradients are detected in the optically thin tracers that could reveal signs of rotation. We suggest that the more likely scenario that can explain the puzzling HNC profiles is the one explored in simulations carried out by Chira et al. (2014). They performed the simulation of a cluster with cores embedded in filaments and make radiative transfer calculations of HCO^+ and HCN in several transitions (not HNC as in our observations). In their simulations, the gas in dense filaments in front of and moving toward a core, red-shifted from the observer line of sight, can be sufficiently dense and emit at low transitions to produce non-blue asymmetries in the observed line profiles (by making the red-shifted peak brighter). According to Chira et al. (2014), in irregular-collapsing cores infall signatures may not be evident in all molecular tracers at a given transition. In our case, HCO^+ shows infall signatures while HNC does not. In order to confirm Chira et al. (2014) predictions in collapsing cores, specific simulations for HNC and observations at higher transitions are necessary.

5. DISCUSSION

5.1. *Prestellar Core Dynamics*

5.1.1. *Virial Equilibrium*

To calculate the virial mass and virial parameter, we used the emission from the optically thin, cold gas tracers N_2D^+ (3-2) and DCO^+ (3-2). We fitted a Gaussian profile to each spectrum across the ALMA1 core. The average values of the velocity dispersion are 0.27 ± 0.03 km s^{-1} for N_2D^+ and 0.27 ± 0.04 km s^{-1} for DCO^+. Using the observed velocity dispersion (σ_v) and the thermal velocity dispersion (σ_{th}) of the deuterated molecules, we can calculate the non-thermal component and assess how turbulent is the gas in the core. The non-thermal velocity dispersion (σ_{nt}) is calculated from $\sigma_v^2 = \sigma_{th}^2 + \sigma_{nt}^2$. The thermal velocity dispersion is given by $\sigma_{th} = (k_B T/\mu m_H)^{1/2}$, with μ the molecular weight. Using the dust temperature of the clump (14 K), for both deuterated molecules $\sigma_{th} = 0.062$ km s^{-1} (same molecular weight, μ). The Mach number ($\sigma_{nt}/\sigma_{th-H_2}$)
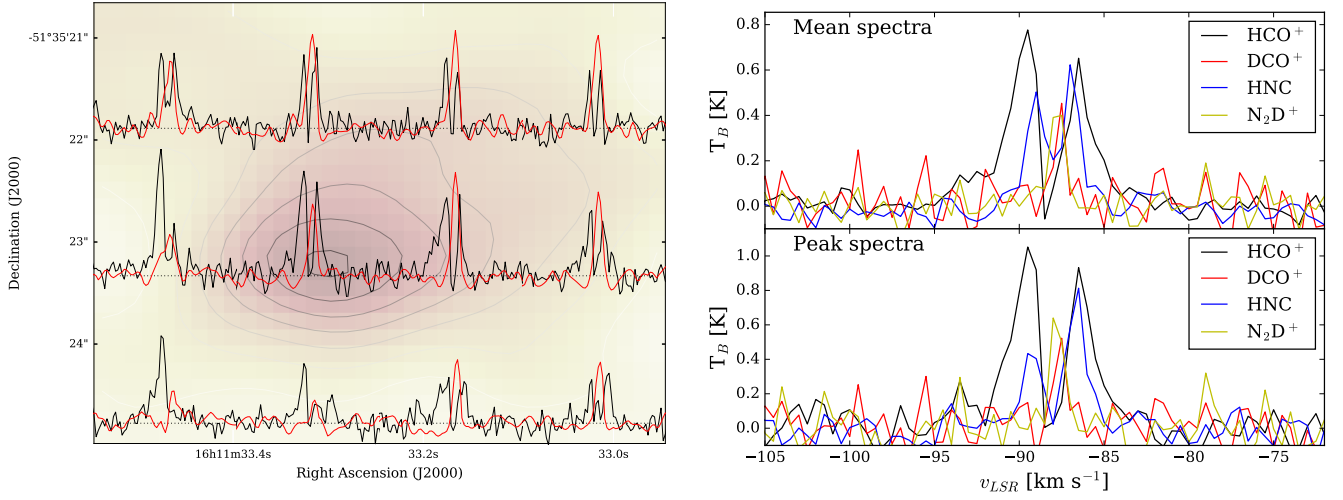
Figure 4. Left: HCO$^+$ (3-2) (black) and C^{18}O (2-1) (red) spectra overlaid to the dust continuum emission observed towards ALMA1. Right upper panel: Mean spectra across ALMA1 of the HCO$^+$ (3-2), DCO$^+$ (3-2), HNC (3-2) and N$_2$D$^+$ (3-2) line emission. Here both optically thin tracers shows a single peak at the position of the v_{LSR} of the core. The HNC mean spectra shows a small red-peaked profile, while HCO$^+$ shows clearly the typical blue-peaked infall profile. Right lower panel: Peak spectra of the same four lines as in the upper panel. Here the infall profile is also evident toward the peak position, while for HNC there is no evidence of infall.

is then 1.19 ($\sigma_{th-H_2} = 0.22$ km s^{-1}), indicating that the gas in the core is transonic.

The virial mass of ALMA1 is calculated using

$$M_{vir} = 3 \left(\frac{5-2n}{3-n} \right) \frac{\sigma_v^2 R}{G}, \qquad (2)$$

where R is the effective radius of the core, G is the gravitational constant, and n is a constant whose value depends on the density profile of the core as function of the radial distance, $\rho(r) \propto r^{-n}$ (MacLaren et al. 1988). Here we adopt a value of $n = 1.8$, which has been found to be representative for high-mass star-forming regions (Mueller et al. 2002; Garay et al. 2007). The virial mass of ALMA1 is derived to be $M_{vir} = 2.4 \pm 0.6$ M$_\odot$, and its virial parameter is $\alpha_{vir} = 0.14 \pm 0.08$, assuming a 50% uncertainty in the mass value. The low value of the virial parameter for ALMA1 suggests that turbulence is insufficient to maintain the stability of ALMA1 (Pillai et al. 2011; Tan et al. 2013; Lu et al. 2015; Zhang et al. 2015; Ohashi et al. 2016; Sanhueza et al. 2017).

It is possible that magnetic fields play a role in the stability of this core (Zhang et al. 2014; Frau et al. 2014). The virial mass taking into account the contribution of a magnetic field support would be given by:

$$M_{B,vir} = 3 \frac{R}{G} \left(\frac{5-2n}{3-n} \right) \left(\sigma_v^2 + \frac{1}{6} \sigma_A^2 \right), \qquad (3)$$

where σ_A is the Alfven velocity, and $n = 1.8$ as in Equation 2. The Alfven velocity is given by $\sigma_A = B/\sqrt{4\pi\rho}$,

where B is the magnitude of the magnetic field and ρ is the core mass density (Sanhueza et al. 2017).

In order to reach virial equilibrium ($M_{B,vir}/M_{core} = 1$), the magnetic field strength in ALMA1 would need to be of the order of 1.2±0.4 mG (assuming a 50% uncertainty in the core's mass). Observations of the magnetic field have not been done toward G331.372-00.116. Such field strengths have been reported in hot molecular cores (Zhang et al. 2014), and recently observed toward prestellar core candidates in the high-mass regime (Beuther et al. 2018).

5.1.2. *A Relatively Massive Starless Core Accreting From Its Environment*

We estimated the core accretion rate from the HCO$^+$ (3-2) molecular line emission. The HCO$^+$ profile is blue peaked, characteristic of infall, toward most of the area defining ALMA1.

To estimate the infall velocity we used the "Hill5" model (De Vries & Myers 2005). "Hill5" is a simple radiative transfer model that can reproduce the observed spectral asymmetries which are expected to arise in a contracting core. In this model, the core has a peak excitation temperature T_{peak} at the center and at the near and far edges of the core it has a excitation temperature T_0. Thus, the core is modeled as a two layer slab, where the excitation temperatures increase linearly up to a peak temperature at the boundary between the two regions (T_{peak}), and then decreases linearly back to

the initial temperature (T_0). For this model the free parameters to fit are (1) the peak excitation temperature (T_{peak}), (2) the velocity dispersion of the molecular line (σ), (3) the optical depth of the line (τ), (4) the velocity of the cloud with respect to the Local Standard of Rest (V_{LSR}), and (5) the infall velocity of the gas in the core (V_{in}). This model may underestimate the infall velocity in some cases. However, the reliability of the model improves when the infall velocity is higher than the velocity dispersion of the line and when the line profile has a separated red-shifted peak. Both conditions met by our observations.

To determine the global accretion rate toward ALMA1, we fitted the average spectrum of the HCO$^+$ emission detected across ALMA1 using Hill5. To perform the fitting, we used the Hill5 model from the PySpecKit[3] spectroscopic analysis toolkit (Ginsburg & Mirocha 2011). PySpecKit uses `lmfit` to perform the fit to the data to the Hill5 model. The uncertainties in the fitting are given by `lmfit` functions that explicitly explore the parameter space and determine confidence levels. As initial guesses of the fit we used τ ranging from 0.1 to 30, a v_{LSR} between -89 and -86.6 km s^{-1}, v_{in} between 0.1 and 4 km s^{-1}, σ between 0.3 and 0.9 km s^{-1}, and T_{peak} between 2 and 30 K. Figure 5 shows the spectra modeled by Hill5. Table 2 shows the values for ALMA1 of the τ, v_{LSR}, v_{in}, σ, and T_{peak} obtained by the model. In this table we also shows the parameters derived from the optically thin tracers detected toward this core.

The mass infall accretion rate of the core was calculated via $\dot{M} = 4\pi R^2 \rho v_{in}$. For ALMA1 its mean density is $\rho = (8.5 \pm 2.7) \times 10^5$ cm^{-3}, $v_{in} = 1.54 \pm 0.03$ km s^{-1} is the mean infall velocity across the core, and R=0.041 pc is its radius. Thus, we estimate a mass infall rate of $(1.96 \pm 0.10) \times 10^{-3}$ M$_\odot$ yr^{-1}, which is an lower limit if we consider that the model can underestimate the infall velocity of the core. This accretion rate is comparable to values measured in high-mass star-forming regions (e.g., Fuller et al. 2005; Sanhueza et al. 2010; Peretto et al. 2013; Liu et al. 2017, 2013)

We compare this value to the simple case of assuming the core as a singular isothermal sphere. In this case the mass accretion rate of the core assuming turbulent motions and a star formation efficiency of 0.3 is given by $\dot{M} \sim 0.441 \sigma^3 / G$ (McKee & Tan 2003), where σ is the HCO$^+$ (3-2) velocity dispersion derived from the Hill5 fit. This simple model gives an accretion rate of $(2.5 \pm 0.4) \times 10^{-5}$ M$_\odot$ yr^{-1}, which is significantly low
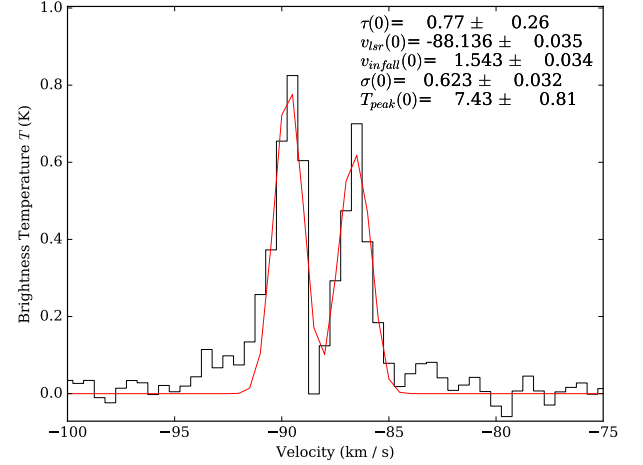
[3] http://pyspeckit.readthedocs.io

Figure 5. Mean HCO$^+$ (3-2) spectrum across ALMA1 (black). In red is shown the Hill5 fit. In the upper right corner is shown the parameters fitted by the model.

compared to the accretion rate obtained from the Hill5 model and to other regions of high-mass star formation (McKee & Tan 2003).

5.1.3. *Prospects for High-Mass Star Formation in IRDC G331.372-00.116*

In spite of having all necessary physical properties to form high-mass stars, IRDC G331.372-00.116 has only one relatively massive core of 17.6 M$_\odot$. This core can be hardly considered a high-mass prestellar core as the core accretion theory predicts (see discussion in Tan et al. 2013, 2014; Sanhueza et al. 2017). Tan (2017) suggests that in a similar IRDC, G028.23-00.19 (Sanhueza et al. 2013, 2017), high-mass cores are absent because they have not yet formed. This could also be the case for G331.372-00.116 and high-mass prestellar cores could eventually form later. However, ALMA1 is a relatively massive, sub-virialized core that has signs of accretion. This accretion can increase the mass of the core, making the scenario observed in IRDC G331.372-00.116 partially consistent with competitive accretion theories (Bonnell et al. 2004; Wang et al. 2010), in which the core increases its mass over time to eventually gather sufficient mass to form a high-mass star.

However, the thermal Jeans mass (M_J) of the IRDC G331.372-00.116, given by

$$M_J = \frac{\pi^{5/2}}{6} \frac{\sigma_{th}^3}{\sqrt{G^3 \rho}} , \qquad (4)$$

is only 2.8 M$_\odot$ (with σ_{th} the thermal velocity dispersion of the gas , dominated by H$_2$ and He, and ρ the clump mass density). Thus, ALMA1 is 6 times more

massive than the Jeans mass, which is high to agree with the competitive accretion theory unless the core has had sufficient time to grow. At the current accretion rate, a core with a Jeans mass would need 7.0×10^3 yr to increase its mass to the current value of ALMA1. Our finding in ALMA1 is consistent with studies of more evolved massive IRDCs by Zhang et al. (2009); Zhang & Wang (2011), and Wang et al. (2014) who report cores of super Jeans masses.

The low turbulence in ALMA1, characterized by a transonic Mach number, results in a low virial parameter that suggests rapid collapse, similar to what is found in other prestellar cores embedded in high-mass star-forming clumps (Sanhueza et al. 2017; Lu et al. 2018). If we take into account magnetic field support, then ALMA1 may be maintained in virial equilibrium as the turbulent core accretion model requires (McKee & Tan 2003). However, the rapid collapse is confirmed at high-angular resolution by the blue-red asymmetry characteristic of collapse. The accretion in ALMA1 is indeed more than 100 times faster than typically measured in low-mass star-forming cores and what is predicted by collapse of an isothermal sphere (McKee & Tan 2003; Shu 1977).

Should magnetic field be negligible, the subvirial state of ALMA1 is supposed to cause collapse and fragmentation. Indeed, it is expected that cores that form high-mass stars will form binary system given that 80% of high-mass stars are found in binary systems (Chini et al. 2012). For ALMA1, the thermal Jeans length corresponds to $\lambda_J = 0.025$ pc. This size is one third of ALMA1 size and it is comparable to the synthesized beam of the observations (1″2, 0.03 pc). Therefore, if ALMA1 collapses it might fragments only into a few cores of roughly the size of the thermal Jeans length.

Whether or not ALMA1 fragments into smaller units, there is a high probability that the core will form at least one high-mass star. For ALMA1 the core free fall time is $t_{ff} = \sqrt{3\pi/(32G\rho)} = 3.3 \times 10^4$ yr. If ALMA1 continue accreting material from its environment, which can be possible given the large reservoir of gas within G331.372-00.116, at its current accretion rate it can grow to reach a ~ 82 M$_\odot$ core on a timescale of its free fall time (assuming a constant accretion rate over the whole time). Thus, it is highly likely that ALMA1 is the initial cocoon of what will be at least one high-mass star in the future.

We suggest that ALMA1 will likely form a high-mass star and that there may be no need to wait for the formation of a high-mass prestellar core in IRDC G331.372-00.116 in order to form a high-mass star. However, there remain two unanswered questions that we are going to

answer in our future studies. First, would ALMA1 indeed fragment at high angular resolution observations? Second, is ALMA1 globally fed by/through filamentary accretion?. We also suggest that cores that will ultimately form high-mass stars begin in a sub-virial state with a low level of turbulence.

6. CONCLUSIONS

We studied the internal structure of the 70 μm dark IRDC G331.372-00.116 with ALMA. Although G331.372-00.116 satisfy all the conditions to form a high-mass star, the most massive core, ALMA1, has only a mass of 17.6 M$_\odot$.

The virial mass of ALMA1 is 2.4±0.6 M$_\odot$ and its virial parameter is 0.14±0.08, suggesting that the core is sub-virial and turbulence alone cannot halt collapse. Table 3 summarizes all the properties derived for ALMA1.

We found evidence of infall toward ALMA1, as shown by the blue-peaked profiles exhibited by HCO$^+$ molecular line emission. Using the Hill5 model we estimated an infall velocity of 1.54±0.03 km s^{-1} and a mass infall accretion rate of $(1.96\pm0.10) \times 10^{-3}$ M$_\odot$ yr^{-1}. If ALMA1 continue to gather material from its environment at the current rate, this core can reach to ~ 82 M$_\odot$ on time scales comparable to the core free-fall time.

Overall, our observations suggest that ALMA1 will likely form a high-mass star, and the starting point for such high-mass star is a sub-virial core of an intermediate mass with low turbulence that will increase it mass via accretion.

CONTRERAS ET AL.

Table 1. Properties of the sub-structures detected towards G331.372-00.116

Core Name	RA (J2000)	DEC (J2000)	Radius (pc)	Peak Flux (mJy beam^{-1})	Integrated Flux (mJy)	N(H$_2$) ($\times 10^{23}$ cm^{-2})	Mass (M$_\odot$)	n(H$_2$) ($\times 10^6$ cm^{-3})	Σ (g cm^{-2})
ALMA1	16:11:33.30	-51:35:23.3	0.041	4.07	25.9	2.95	17.6	0.85	0.65
ALMA2	16:11:32.68	-51:35:21.2	0.019	1.62	3.27	1.18	2.22	1.19	0.41
ALMA3	16:11:34.64	-51:35:17.1	0.013	1.13	1.30	0.81	0.88	1.38	0.33
ALMA4	16:11:33.14	-51:35:17.1	0.014	1.65	2.36	1.20	1.60	1.83	0.49
ALMA5	16:11:33.31	-51:35:15.1	0.019	1.46	2.83	1.06	1.92	0.97	0.34
ALMA6	16:11:33.93	-51:35:10.2	0.023	1.51	4.81	1.09	3.26	0.88	0.38
ALMA7	16:11:33.43	-51:35:10.5	0.018	1.64	3.39	1.19	2.30	1.37	0.45
ALMA8	16:11:33.14	-51:35:09.7	0.012	1.32	1.30	0.95	0.88	1.70	0.38
ALMA9	16:11:34.04	-51:35:04.1	0.030	1.65	6.84	1.19	4.64	0.59	0.33
ALMA10	16:11:34.05	-51:34:59.5	0.034	2.59	10.9	1.88	7.40	0.66	0.41
ALMA11	16:11:34.46	-51:34:56.4	0.014	1.31	1.66	0.95	1.13	1.43	0.37
ALMA12	16:11:33.85	-51:34:54.0	0.017	1.29	1.97	0.93	1.34	0.87	0.28
ALMA13	16:11:34.36	-51:34:53.7	0.012	1.13	1.20	0.82	0.81	1.56	0.35
ALMA14	16:11:34.84	-51:34:50.7	0.019	1.25	2.52	0.91	1.71	0.90	0.31
ALMA15	16:11:34.29	-51:34:51.1	0.014	1.26	1.71	0.91	1.16	1.32	0.35
ALMA16	16:11:34.05	-51:34:51.0	0.017	1.45	2.42	1.05	1.64	1.24	0.38
ALMA17	16:11:33.28	-51:34:50.5	0.015	3.01	3.82	2.18	2.60	2.55	0.71
ALMA18	16:11:33.64	-51:34:49.5	0.017	2.09	3.63	1.52	2.47	1.80	0.56
ALMA19	16:11:34.88	-51:34:48.7	0.013	1.65	1.75	1.20	1.19	1.98	0.46
ALMA20	16:11:34.02	-51:34:46.7	0.041	2.06	15.7	1.49	10.7	0.54	0.41
ALMA21	16:11:33.43	-51:34:36.3	0.019	1.23	2.78	0.89	1.88	0.94	0.33
ALMA22	16:11:32.61	-51:34:34.7	0.041	1.60	13.9	1.16	9.42	0.46	0.35

Table 2. Summary of the line parameters of the optically thin tracers observed towards ALMA1, and the derived parameters from the Hill5 model.

		τ	v_{in} (km s^{-1})	T$_{peak}$ (K)	σ (km s^{-1})	v_{LSR} (km s^{-1})	Method
HCO$^+$	J=3-2	0.77±0.26	1.54±0.03	7.43±0.81	0.62±0.03	-88.14±0.04	Hill5
N$_2$D$^+$	J=3-2			0.91±0.09	0.27±0.03	-87.69±0.03	Gaussian Fit
DCO$^+$	J=3-2			0.66±0.08	0.27±0.04	-87.71±0.04	Gaussian Fit
C^{18}O	J=2-1			0.67±0.05	0.68±0.06	-87.37±0.06	Gaussian Fit

Table 3. Summary of physical parameter derived for ALMA1

Parameter	Value
Flux (267 GHz)	26 mJy
r_{eff}	0.041±0.004 pc
M	17.6±8.8 M$_\odot$
M_{vir}	2.4±0.6 M$_\odot$
α_{vir}	0.14±0.08
n(H$_2$)	(8.5±2.7)×10^5 cm^{-3}
Σ	0.65 gr cm^{-2}
$\mathcal{M}$	1.19
$\dot{M}$	(1.96±0.10)×10^{-3} M$_\odot$ yr^{-1}
t$_{ff}$	3.3×10^4 yr

Facilities: ALMA

Software: CASA 4.7.2

REFERENCES

Beuther, H., Soler, J., Vlemmings, W., et al. 2018, ArXiv e-prints, arXiv:1802.00005

Bonnell, I. A., Bate, M. R., Clarke, C. J., & Pringle, J. E. 2001, MNRAS, 323, 785

Bonnell, I. A., Vine, S. G., & Bate, M. R. 2004, MNRAS, 349, 735

Carey, S., Noriega-Crespo, A., Price, S., et al. 2005, in Spitzer Proposal ID #20597, 20597–+

Chini, R., Hoffmeister, V. H., Nasseri, A., Stahl, O., & Zinnecker, H. 2012, MNRAS, 424, 1925

Chira, R.-A., Smith, R. J., Klessen, R. S., Stutz, A. M., & Shetty, R. 2014, MNRAS, 444, 874

Churchwell, E., Babler, B. L., Meade, M. R., et al. 2009, PASP, 121, 213

Contreras, Y., Rathborne, J. M., Guzman, A., et al. 2017, MNRAS, 466, 340

Contreras, Y., Schuller, F., Urquhart, J. S., et al. 2013, A&A, 549, A45

Cyganowski, C. J., Brogan, C. L., Hunter, T. R., et al. 2014, ApJL, 796, L2

De Vries, C. H., & Myers, P. C. 2005, ApJ, 620, 800

Foster, J. B., Jackson, J. M., Barnes, P. J., et al. 2011, ApJS, 197, 25

Foster, J. B., Rathborne, J. M., Sanhueza, P., et al. 2013, PASA, 30, e038

Frau, P., Girart, J. M., Zhang, Q., & Rao, R. 2014, A&A, 567, A116

Fuller, G. A., Williams, S. J., & Sridharan, T. K. 2005, A&A, 442, 949

Garay, G., Mardones, D., Brooks, K. J., Videla, L., & Contreras, Y. 2007, ApJ, 666, 309

Ginsburg, A., & Mirocha, J. 2011, PySpecKit: Python Spectroscopic Toolkit, Astrophysics Source Code Library, , , ascl:1109.001

Guzmán, A. E., Sanhueza, P., Contreras, Y., et al. 2015, ApJ, 815, 130

Jackson, J. M., Rathborne, J. M., Foster, J. B., et al. 2013, PASA, 30, 57

Kauffmann, J., Bertoldi, F., Bourke, T. L., Evans, II, N. J., & Lee, C. W. 2008, A&A, 487, 993

Kong, S., Tan, J. C., Caselli, P., et al. 2017, ArXiv e-prints, arXiv:1701.05953

Kroupa, P. 2001, MNRAS, 322, 231

Krumholz, M. R. 2012, in Astronomical Society of the Pacific Conference Series, Vol. 464, Circumstellar Dynamics at High Resolution, ed. A. C. Carciofi & T. Rivinius, 339

Larson, R. B. 2003, in Astronomical Society of the Pacific Conference Series, Vol. 287, Galactic Star Formation Across the Stellar Mass Spectrum, ed. J. M. De Buizer & N. S. van der Bliek, 65–80

Liu, T., Wu, Y., Wu, J., Qin, S.-L., & Zhang, H. 2013, MNRAS, 436, 1335

Liu, T., Zhang, Q., Kim, K.-T., et al. 2016, ApJ, 824, 31

Liu, T., Lacy, J., Li, P. S., et al. 2017, ApJ, 849, 25

Lu, X., Zhang, Q., Wang, K., & Gu, Q. 2015, ApJ, 805, 171

Lu, X., Zhang, Q., Liu, H. B., et al. 2018, ArXiv e-prints, arXiv:1801.05955

MacLaren, I., Richardson, K. M., & Wolfendale, A. W. 1988, ApJ, 333, 821

McKee, C. F., & Tan, J. C. 2003, ApJ, 585, 850

McMullin, J. P., Waters, B., Schiebel, D., Young, W., & Golap, K. 2007, in Astronomical Society of the Pacific Conference Series, Vol. 376, Astronomical Data Analysis Software and Systems XVI, ed. R. A. Shaw, F. Hill, & D. J. Bell, 127

Mueller, K. E., Shirley, Y. L., Evans, II, N. J., & Jacobson, H. R. 2002, ApJS, 143, 469

Nguyễn, H., Nguyễn Lu'o'ng, Q., Martin, P. G., et al. 2015, ApJ, 812, 7

Ohashi, S., Sanhueza, P., Chen, H.-R. V., et al. 2016, ApJ, 833, 209

Ossenkopf, V., & Henning, T. 1994, A&A, 291, 943

Peretto, N., Fuller, G. A., Duarte-Cabral, A., et al. 2013, A&A, 555, A112

Pillai, T., Kauffmann, J., Wyrowski, F., et al. 2011, A&A, 530, A118

Rathborne, J. M., Whitaker, J. S., Jackson, J. M., et al. 2016, PASA, 33, e030

Redman, M. P., Rawlings, J. M. C., Yates, J. A., & Williams, D. A. 2004, MNRAS, 352, 243

Rosolowsky, E. W., Pineda, J. E., Kauffmann, J., & Goodman, A. A. 2008, ApJ, 679, 1338

Sanhueza, P., Garay, G., Bronfman, L., et al. 2010, ApJ, 715, 18

Sanhueza, P., Jackson, J. M., Foster, J. B., et al. 2012, ApJ, 756, 60

—. 2013, ApJ, 773, 123

Sanhueza, P., Jackson, J. M., Zhang, Q., et al. 2017, ApJ, 841, 97

Shu, F. H. 1977, ApJ, 214, 488

Tan, J. C. 2017, ArXiv e-prints, arXiv:1710.11607

Tan, J. C., Beltrán, M. T., Caselli, P., et al. 2014, Protostars and Planets VI, 149

Tan, J. C., Kong, S., Butler, M. J., Caselli, P., & Fontani, F. 2013, ApJ, 779, 96

Wang, K., Zhang, Q., Testi, L., et al. 2014, MNRAS, 439, 3275

Wang, P., Li, Z.-Y., Abel, T., & Nakamura, F. 2010, ApJ, 709, 27

Whitaker, J. S., Jackson, J. M., Rathborne, J. M., et al. 2017, AJ, 154, 140

Zhang, Q., & Wang, K. 2011, ApJ, 733, 26

Zhang, Q., Wang, K., Lu, X., & Jiménez-Serra, I. 2015, ApJ, 804, 141

Zhang, Q., Wang, Y., Pillai, T., & Rathborne, J. 2009, ApJ, 696, 268

Zhang, Q., Qiu, K., Girart, J. M., et al. 2014, ApJ, 792, 116

APPENDIX

A. AUTOMATIC CLEANING ALGORITHM

We have developed an automatic cleaning algorithm for imaging data cubes, `yclean`. The algorithm is written in `python` and make use of the `tclean` task in the CASA software. `yclean` creates individual masks for every channel of a line data set through an iterative process in order to obtain the optimal mask per channel for cleaning.

The `yclean` algorithm determines a threshold to mask every channel that depends on the value of the secondary lobe of the PSF, the rms of the image, and the maximum value of the image residual. First, it creates a dirty beam image with the `tclean` task in CASA. From the dirty .psf image, the algorithm determines the value of the secondary lobe (`secondaryLobe`) of the PSF map. From the .im image, it calculates the rms of the map (`rmsMap`) by computing the average rms value (using CASA `imstat` task) of a subset of channels located in a line free region of the map (usually near the edges of the spectral window). Finally, from the .residual image we obtain the maximum value (`maxResidual`). With the values of `secondaryLobe`, `rmsMap`, and `maxResidual`, a threshold is defined to create a mask that will be used with `tclean` (`limitLevelSNR`).

The `limitLevelSNR` is given by:

$$\texttt{limitLevelSNR} = \frac{\texttt{maxResidual}}{\texttt{rmsMap} \times \texttt{secondaryLobe}} \tag{A1}$$

After computing the first mask, a loop begins that finishes when the measured value of `limitLevelSNR` is greater than 2. In each loop, the following actions are performed:

- Create a mask.

- Combine the new mask with the mask used in the previous iteration.

- Use `tclean` to clean the image using the mask previously created. In this step, the image is cleaned until it reaches a threshold given by `limitLevelSNR`×`rmsMap`.

- Calculate a new value of `limitLevelSNR`.

Once the loop ends, the `yclean` script performs a final clean using `tclean` with a cleaning stopping threshold given by 2×`rmsMap` and using a final mask that combines the previous mask with a new mask created with a threshold of 4×`rmsMap`. Finally, after the cleaning is done, all the products are exported into fits format.

More documentation about the `yclean` script, along with the necessary modules to run it, are available at www.yanettcontreras.com/yclean.html. A frozen version of the script can also be found at zenodo (10.5281/zenodo.1216881).